ACS APPLIED NANO MATERIALS

www.acsanm.org

Article

Poly(sobrerol methacrylate) Colloidal Inks Sprayed onto Cellulose Nanofibril Thin Films for Anticounterfeiting Applications

Constantin Harder, Marie Betker, Alexandros E. Alexakis, Yusuf Bulut, Benedikt Sochor, L. Daniel Söderberg, Eva Malmström, Peter Müller-Buschbaum, and Stephan V. Roth*

Cite This: *ACS Appl. Nano Mater.* 2024, 7, 10840−10851

Read Online

ACCESS | Metrics & More | Article Recommendations | Supporting Information

ABSTRACT: The colloidal layer formation on porous materials is a crucial step for printing and applying functional coatings, which can be used to fabricate anticounterfeiting paper. The deposition of colloidal layers and subsequent thermal treatment allows for modifying the hydrophilicity of the surface of a material. In the present work, wood-based colloidal inks are applied by spray deposition on spray-deposited porous cellulose nanofibrils (CNF) films. The surface modification by thermal annealing of the fabricated colloid-cellulose hybrid thin films is investigated in terms of layering and hydrophobicity. The polymer colloids in the inks are core−shell nanoparticles with different sizes and glass transition temperatures (T_g), thus enabling different and low thermal treatment temperatures. The ratio between the core polymers, poly(sobrerol methacrylate) (PSobMA), and poly(-butyl methacrylate) (PBMA) determines the T_g and hence allows for tailoring of the T_g. The layer formation of the colloidal inks on the porous CNF layer depends on the imbibition properties of the CNF layer which is determined by their morphology. The water adhesion of the CNF layer decreases due to the deposition of the colloids and thermal treatment except for the colloids with a size smaller than the void size of the porous CNF film. In this case, the colloids are imbibed into the CNF layer when T_g of the colloids is reached and the polymer chains transit in a mobile phase. Tailored aggregate and nanoscale-embedded hybrid structures are achieved depending on the colloid properties. The imbibition of these colloids into the porous CNF films is verified with grazing incidence small-angle X-ray scattering. This study shows a route for tuning the nanoscale structure and macroscopic physicochemical properties useful for anticounterfeiting paper.

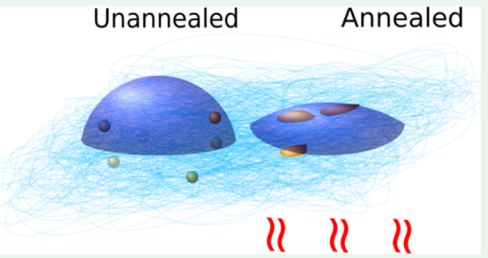

KEYWORDS: *cellulose nanofibrils, thin films, wetting, colloids, colloidal films, surface energy, GISAXS*

INTRODUCTION

Hybrid porous thin films, composed of a porous template and polymer or inorganic colloids, have found diverse applications across various fields due to their unique properties.[1] These films are used for flexible electronics in flexible photovoltaics or sensors,[2] fabricating membranes, e.g., to filter water from dust, salt, or heavy metals,[3] or anticounterfeiting materials.[4,5] The macroscopic properties required for these applications are inherently determined by the hybrid materials' morphologies; for example, they influence surface energy. The surface energy directly affects the usability of the porous thin films because it influences the surface's water adhesion and solvent imbibition properties of porous films.[6,7] Depending on the material's topology, the morphology changes during a treatment.[8,9] Both the deposition of colloids and the annealing process above a critical temperature alter the morphology of a material.[10] Therefore, incorporating colloids into the network of porous cellulose nanofibrils (CNF) is suitable for modifying water adhesion.[11] Embedded nanoparticles give the hybrid material different properties than surface nanoparticles.[12,13]

The modified water adhesion is usable as a direct nonvisible eye feature for anticounterfeiting, where the water adhesion shows if the surface was correctly treated.[14,15]

Spray-coated CNF layers with a high surface energy and a high degree of homogeneity with a defined porosity and roughness are used.[16−18] This results in specific imbibition properties of different materials and solvents in the CNF layer.[12,19]

For instance, CNF derived from wood biomass is biodegradable, sustainable by regrowth, and can serve as lightweight and flexible nanoscopic building blocks.[20−22] CNF is a bundle of several glucose $(C_6H_{10}O_5)_{n+2}$ chains.[23] 2,2,6,6-Tetramethylpiperidine-1-oxyl (TEMPO)-mediated oxidized CNF is functionalized by surface charges. A single CNF is approximately 3−5 nm in diameter and 500−1000 nm in length, depending on the surface charge.[16,24] The characteristics of thin

Received: March 5, 2024
Revised: April 17, 2024
Accepted: April 19, 2024
Published: April 30, 2024

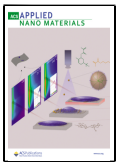

Table 1. Characteristics of the Used Colloids[31,40]

name	BMA:SobMA	T_g [°C]	hydrodynamic radius R_H [nm]	radius size (AFM)[31,40] [nm]	stabilization
$PSobMA_{CTAC}$		123 ± 2	55 ± 1	38 ± 12	CTAC
$P(SobMA\text{-}co\text{-}BMA)_{CTAC}$	83:17	50 ± 2	55 ± 3	41 ± 10	CTAC
$P(SobMA\text{-}co\text{-}BMA)_{1000}$	50:50	74 ± 2	44 ± 1	29 ± 6	PDMAEMA

CNF films, water adhesion, or imbibition properties are governed by the morphology which is given by the surface charge of CNF and the arrangement of the fibrils.[21,25,26] The CNF layer is not allowed to undergo any morphological changes below an annealing temperature of 200 °C.[27] CNF forms a long-range network that serves as a good template or carrier for nanoparticles, making it useful for various applications such as anticounterfeiting or as a holder for electronic devices.[12,13,28−30]

Sobrerol methacrylate (SobMA) is used to synthesize wood-based colloids on the hydration of α-pinene oxide.[31] It is produced sustainably, providing similar glass transition temperature (T_g) and hydrophobic properties as the fossil fuel-produced PMMA or PS colloids, making it a sustainable alternative.[31] To fabricate monodisperse colloids, polymerization-induced self-assembly (PISA) coupled with reversible addition−fragmentation chain-transfer (RAFT) polymerization is employed to fabricate monodisperse colloids.[32] The hydrophobic polymer PSobMA is combined with a hydrophilic polymer block of poly(2-(dimethylamino)ethyl methacrylate (PDMAEMA)) or stabilized by the cationic surfactant cetyltrimethylammonium chloride (CTAC). This results in core−shell particles, the core of which is shielded by a hydrophilic corona. PDMAEMA or CTAC, respectively, define the shell properties of the SobMA-based colloids and enable the suspension of the colloids in water, as an ideal green and nontoxic carrier.[33] The main characteristics of the colloid, such as T_g, electromagnetic properties, and/or photonic characteristics, are determined by the core. The focus feature of the colloids in this work is the T_g. Polybutyl methacrylate (PBMA) is used to tune the T_g of the colloids.[34]

The primary objective of the study is to investigate the alteration of surface energy through the deposition of biobased colloids, followed by an annealing process. Correlating changes in water adhesion with the morphological differences between pristine CNF thin films and CNF-colloid hybrid materials, both with and without subsequent annealing, constitutes our first aim. The second aim is to establish a correlation between alterations in surface energy and morphological changes.

The layer morphology of the colloids on and within the CNF matrix is analyzed using grazing incidence small-angle X-ray scattering (GISAXS) and atomic force microscopy (AFM). GISAXS serves as a sensitive tool for assessing both surface and bulk morphology. The third aim is to demonstrate that GISAXS is a valuable tool for verifying the imbibition of biobased colloids into a porous cellulose matrix, showcasing the sensitivity of GISAXS to changes in bulk state.[35]

While the impact of colloids on the surface energy of solid material is known,[34,36] the specific effects of SobMA-based colloids on the surface energy of porous CNF layers are still unknown. Similarly, while it is known that water can penetrate the CNF layer,[37] the question of whether colloids can infiltrate the cellulose matrix is still unanswered. To investigate this, colloids of different sizes, including those larger and smaller than the CNF voids, are used in the study.

EXPERIMENTAL SECTION

Cellulose Nanofibrils (CNF). CNF are wood-based with a diameter of around 5 nm and a length between 500 and 1000 nm.[24] TEMPO-mediated treatment oxidizes the free CH_2OH group to a COOH group,[22] (Supporting Information Figure S1a). CNF with a surface charge of 1000 μmol/g has the highest surface energy, ≈73 mN/m.[16] To fabricate these CNF layers, a gel-like CNF dispersion is used. This dispersion is diluted with water to a 0.07 wt % and treated by mechanical mixing (12,800 rpm, 10 min, Ultra Turrax, IKA, Germany) and sonication (10 min, Bandelin Sonopuls HD/UW 2070, Germany) and finally centrifuged (5000 rpm, 60 min, Rotina 420, Hettich GmbH & Co. KG, Germany). The CNF suspension is then spray-coated on 20 × 20 mm^2 polished and acidly cleaned silicon (Si) wafers (Boron-doped, (100) orientation, Si-Mat, Germany). For spray deposition of the CNF on the cleaned Si wafer, a distance of 200 mm between the spray device (Compact JAU D55000, Spray Systems, Germany) and the wafer is used.[16] A pressure of p = 1 bar for the carrier gas (Nitrogen, purity = 5.0) is used. During deposition, the silicon wafer is heated to 80 °C (set point 120 °C, heating plate VWR VHP C7), and the CNF suspension is spray-deposited iteratively 20 times on the heated substrate. Each spray pulse has a duration of 0.2 s. One spray cycle is complete when the water is completely evaporated, which takes place within 2 s. The time between two cycles is set to 5 s to ensure that water is always completely evaporated between two cycles. The spray-deposited CNF layer forms a specific CNF network. The CNF network is visible in optical microscopy and AFM, see Figure S1b,c. The characteristic thickness of a 150 nm CNF layer[38] on the Si wafer results in blue color. The closely packed morphology, the void structure, and the buildup of the network have been shown in previous works.[16] Three structures in a spray-deposited CNF layer of 20 spray cycles which corresponds to a thickness of 150 ± 10 nm are identifiable from the GISAXS pattern in Figure S1d. These nanostructures are identified as agglomerations (green curve) with a radius size of 7.5 ± 2.3 nm, a void structure radius size (magenta curve) of 30 ± 14 nm, and larger agglomerations radius size (yellow curve) of 100 ± 40 nm. The void structure and the agglomeration agree with Brett et al.[16]

Colloids. The colloids are based on sobrerol which is derived from the terpene α-pinene extracted from birch bark and synthesized to poly(sobrerol methacrylate) (PSobMA).[31] These colloids are characterized by their different glass transition temperatures (T_g) and radius sizes, see Table 1. These spherical, biobased colloids are comparable to previous work on poly(methyl methacrylate) colloids concerning the size used by Engström et al.[34] The radii measured by AFM of the colloids are comparable to the void size of the CNF network. $P(SobMA\text{-}co\text{-}BMA)_{1000}$ colloids are smaller (radius ∼19 nm)[31] and ($PSobMA_{CTAC}$), $P(SobMA\text{-}co\text{-}BMA_{CTAC})$ colloids are larger (radius ∼38 nm and ∼41 nm, respectively)[31] than the void structure size inside the sprayed CNF films.[16] To adjust the T_g of the colloids, SobMA is mixed with butyl methacrylate (BMA, T_g = 36 °C).[39] To fabricate the $P(SobMA\text{-}co\text{-}BMA)_{1000}$ colloids controlled radical polymerization-induced self-assembly (PISA) is used in combination with poly(2-(dimethylamino)ethyl methacrylate) (PDMAEMA) for the shell of the core−shell colloids.[31] The ($PSobMA_{CTAC}$) and $P(SobMA\text{-}co\text{-}BMA_{CTAC})$ colloids are synthesized via emulsion polymerization with CTAC as a cationic surfactant for the shell. The name of the aforementioned polymers includes either CTAC or 1000 as a subscript to indicate their synthesis process. 1000 denotes the targeted degree of polymerization of the hydrophobic blocks when PISA was used. PSobMA and PBMA are both hydrophobic polymers. The used colloidal ink concentration is 0.1 wt % in an aqueous environment.

To deposit the colloids on the CNF layer the identical spray deposition setup including the nozzle type for the deposition of the

https://doi.org/10.1021/acsanm.4c01302
ACS Appl. Nano Mater. 2024, 7, 10840−10851

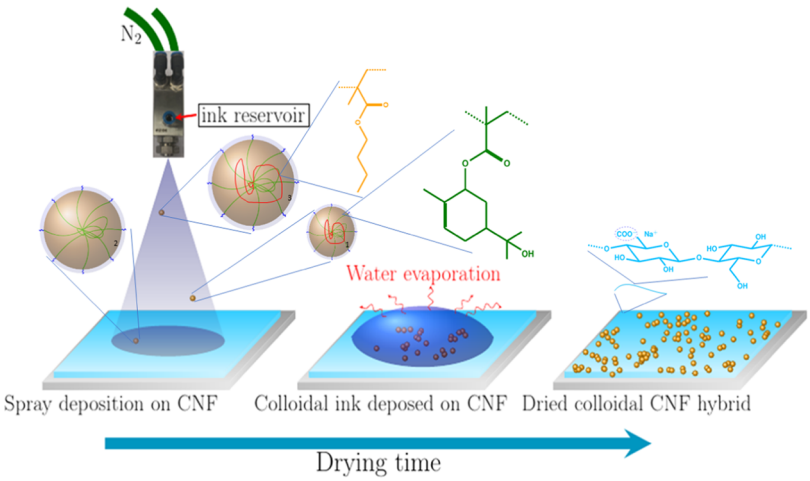

Figure 1. Sketch of the colloidal layer formation on the CNF layer. First, the colloidal ink will be applied to the CNF layer (light blue) by spray deposition. This results in an aqueous colloidal ink film on the CNF layer. The water evaporates with time, and the colloidal layer is formed through evaporation-induced self-assembly. The three different colloid types used in the study are symbolized by the colloids ($1 \triangleq P(SobMA\text{-}BMA)_{1000}$, $2 \triangleq (PSobMA_{CTAC})$, and $3 \triangleq P(SobMA\text{-}BMA)_{CTAC}$). They consist of sobrerol methacrylate (SobMA) [green], butyl methacrylate (BMA) [orange], and their hydrophilic shell (the connection between the core and shell is presented in Figure S2).

CNF layer is used. The colloidal layer is spray-deposited using eight spray pulses with a spraying time of 50 ms. The time between two spray pulses is larger than the time for the evaporation of the water. The time between two pulses is set to 300 s to ensure that the water is completely evaporated. The substrate is kept at room temperature $T \approx 25$ °C, the waiting time is in the minute regime, and the environmental humidity is RH ≈ 35%. The concentration of the colloidal ink is 0.1 wt %. The distance between the spray device and the sample is 200 mm.[34] The deposition process is depicted in Figure 1.

Optical Microscopy. Optical microscopy is performed by a Keyence VHX600 (Keyence corporation, Japan) with a magnification of 2500.

Atomic Force Microscopy (AFM). NTEGRA probe Nano-Laboratory (NT-MDT) in tapping mode with HA_NC tips (ETALON) with a resonance frequency of 140 kHz is scanning the film surface. The data are analyzed with Gwyddion (v2.56).[41]

Contact Angle Measurements. Typically contact angle measurements are used to deduce surface energies.[42] The contact angle was measured with an OCA35(Data Physics, Germany) contact-angle-measuring system. The volume of each water droplet is approximately 5 μL. Each measurement was repeated three times. The measurements and the analysis of the contact angle are performed by the SCA20 (Data Physics, Germany) software. The surface energy E_s is determined from the contact angle θ:[43]

$$E_s = \frac{\gamma_l}{4}(1 + \cos(\theta))^2 \quad (1)$$

For the water interphase, γ_l is given by 72.75 mN/m.

Grazing Incidence Small-Angle X-ray Scattering (GISAXS). GISAXS measurements are performed at the beamline P03 at PETRA III, DESY using a photon energy of $E = 11.8$ keV and an incident angle of $\alpha_i = 0.4°$. For the $P(SobMA\text{-}co\text{-}BMA)_{1000}$ colloids, a sample-to-detector distance of 3930 mm, and for the $P(SobMA\text{-}co\text{-}BMA)_{CTAC}$ and $P(SobMA\text{-}co\text{-}BMA)_{CTAC}$ colloids the sample-to-detector distance of 9530 mm is used. An X-ray beam size of 35 × 30 μm^2 is used. The detector is a PILATUS 300k detector (Dectris Ltd., Switzerland) with a pixel size of 172 × 172 μm^2. The in situ annealing GISAXS experiment with applied temperature started 5 min after achieving the temperature equilibrium (ambient ≡ 25, 40, 70, 100, 140 °C) to directly observe the effect of the applied temperature on the nanostructure. The target temperatures are achieved after ∼0, ∼25, ∼42, ∼58, and ∼74 min (ambient), respectively. To observe the continuous drying process without beam damage, the X-ray beam is continuously scanned laterally over 14 mm (center ±7 mm). Acquisition time per GISAXS image is 0.1 s. The annealing process is similarly observed with an acquisition time of the detector of 0.1 s while scanning over 14 mm with a step width of 0.5 mm. The details for the GISAXS analysis are in the Supporting Information. The scattering length densities (SLD) are calculated in Table S1.

RESULTS AND DISCUSSION

The topologies of colloids and the CNF layer govern the morphological changes of the colloids during both the spray and annealing processes. Consequently, the topologies of the colloids and the CNF layer are unaffected during both the spray and annealing processes. The colloid topology dictates that the colloids initially exhibit a spherical shape, which transitions to an unspecified shape upon reaching their glass transition temperature (T_g). Meanwhile, the CNF topology governs the arrangement of fibrils within the CNF layer, with a void size of approximately 30 nm observed for spray-coated CNF.

Moreover, the objective is to comprehend the topological principles governing both colloids and the CNF layer, deduced from the morphological changes observed during particle annealing. The CNF layer's topology allows only colloids with sizes smaller than the CNF voids, exemplified by the $P(SobMA\text{-}co\text{-}BMA)_{1000}$ colloids, to penetrate during the deposition and evaporation process. Colloids larger than the voids, such as $PSobMA_{CTAC}$ and $P(SobMA\text{-}co\text{-}BMA)_{CTAC}$ colloids, face hindrance in penetration.

The morphological changes in the colloidal CNF hybrid sample significantly impact surface energy. Water adhesion on a surface is contingent on the surface energy of that particular surface. Therefore, understanding the morphology and the raw material contributing to the surface is crucial. Observing the morphology of colloid−CNF hybrid thin films aids in comprehending the alterations in surface energy following the spray coating of colloidal inks onto the hydrophilic CNF.

The adhesion of water on pristine CNF thin films and Si wafers is modified by the deposition of a colloidal layer on top of the pristine CNF layer. The results are depicted in Figure 2 and Table S2. Contact angle measurements are presented in the Supporting Information, Figure S7, with the corresponding values listed in Table S2. The pristine CNF film on Si, as well as the cleaned Si wafer, exhibits the highest surface energy: The

https://doi.org/10.1021/acsanm.4c01302
ACS Appl. Nano Mater. 2024, 7, 10840−10851

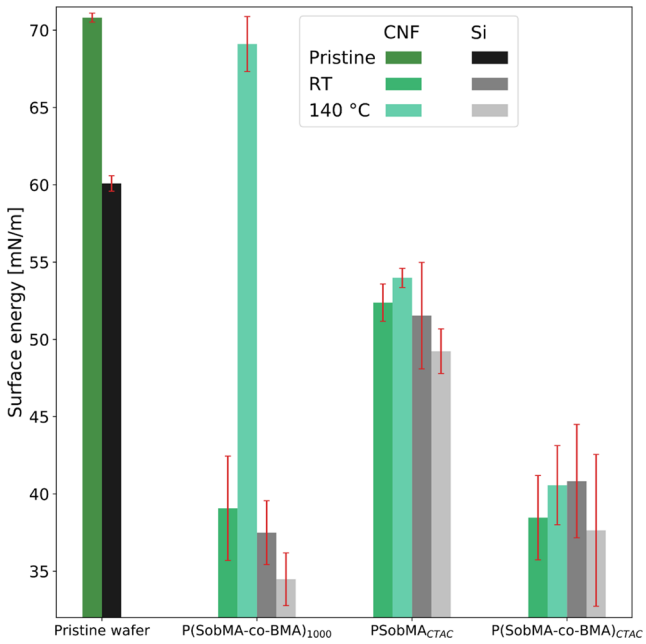

Figure 2. Surface energies are determined over water contact angle measurements of the pristine CNF layer, the silicon wafer (Si), and the deposited colloids on the CNF and Si wafer before and after annealing. The pristine CNF layer and Si wafer show a high surface energy of $70 \pm 1 \frac{mN}{m}$ and acid-cleaned $60 \pm 1 \frac{mN}{m}$, respectively. Through the deposition of the colloids, the surface energy is decreased. After the annealing at 140 °C, the surface energy is increased for the colloid−CNF hybrid thin films (green colors) and decreased for the pure colloidal layers (black and gray colors).

surface energy of CNF with a surface charge of −1000 μmol/g is 70 ± 1 mN/m, and for acid-cleaned silicon, it is 60 ± 1 mN/m (see Figure 2). This indicates strong hydrophilicity, with contact angles of 13 ± 1 and 35 ± 1° for the pristine substrates. After the spray deposition of all colloid types ($PSobMA_{CTAC}$, $P(SobMA\text{-}co\text{-}BMA)_{1000}$, $P(SobMA\text{-}co\text{-}BMA)_{CTAC}$) on CNF and bare silicon, the surface energy decreases (see Table 2).

Table 2. Values of the Surface Energy of the Colloid−CNF Layers

colloids	surface energy CNF [mN/m]	surface energy Si [mN/m]	surface energy CNF [mN/m]	surface energy Si [mN/m]
	ambient	ambient	annealed	annealed
$P(SobMA\text{-}co\text{-}BMA)_{1000}$	38 ± 3	37 ± 3	69 ± 2	34 ± 2
$PSobMA_{CTAC}$	52 ± 2	52 ± 4	54 ± 1	50 ± 2
$P(SobMA\text{-}co\text{-}BMA)_{CTAC}$	39 ± 4	41 ± 4	41 ± 3	38 ± 5

This behavior is similar to the decrease in surface energy observed with PMMA-based and PBMA colloids when spray-deposited on a bare silicon wafer. After applying the colloids on the CNF surface, the water droplet during the contact angle measurement interacts partially with the CNF surface and partially with the colloids. Therefore, the hydrophobic core of the colloids contributes to a decrease in surface energy.

The annealing process on the CNF-colloid layers induces opposite trends in surface energy, increasing. The annealing process also decreases the contact angle on the solid Si wafer (see the evolution of the darker gray to lighter gray columns in Figure 2). Remarkably, the surface energy of the $P(SobMA\text{-}co\text{-}BMA)_{1000}$-CNF hybrid material increased nearly to the initial pristine CNF surface energy during the annealing process (see Supporting Information Table S2). This demonstrates the influence of shell chemistry and imbibition of the colloids on the surface properties of the colloid−CNF hybrid thin films. $P(SobMA\text{-}co\text{-}BMA)_{1000}$, stabilized by a hydrophilic block and not by CTAC as a low-molecular-weight surfactant, has a diameter similar to the void size in the CNF network, allowing it to easily move into the CNF network. Thus, the wetting properties seem to be mainly governed by the CNF and additionally by the hydrophilic block. These results are useful for a quick check to determine the types of colloids applied to the CNF surface and whether the CNF-colloidal hybrid materials are annealed.

The surface topography confirming the presence of colloids on the CNF surface after spray deposition is illustrated in Figure 3. All colloids ($PSobMA_{CTAC}$, $(PSobMA\text{-}co\text{-}BMA)_{1000}$, $P(SobMA\text{-}co\text{-}BMA)_{CTAC}$) display a random distribution on the CNF template (Figure 3a−c), forming agglomerations of individually distinguishable colloids.

Upon annealing at 140 °C, the T_g of the P(SobMA-*co*-BMA)1000 and P(SobMA-*co*-BMA)CTAC colloids is surpassed. This thermal annealing triggers a transformation of colloidal spheres into oblate shapes due to the mobility of the core polymer.[34,44] During annealing, both individual colloids and their agglomerates coalesce, making individual colloids indistinguishable. In contrast, the shape and size of PSobMACTAC colloids remain unchanged after 10 min of annealing at 140 °C.

The coalescence of colloids explains the reduction in surface energy following thermal treatment on the Si wafer (see Supporting Information, Figure S8). The polymer chains undergo rearrangement within the thin film during annealing. This behavior of PSobMA-based colloids mirrors that of PMMA and PBMA colloids on Si.[34] As the annealing process progresses, polymer chains gain mobility, exceed the T_g, and lead to rearranged chains that are more strongly oriented at the air−polymer interface of the colloids, resulting in a more hydrophobic deposited layer. The coalescence of colloids contributes to the observed lower surface energy.

A PMMA-cellulose system, through annealing at 160 °C, increases surface energy by reducing surface roughness.[45] PSobMA, sharing similarities with PMMA in terms of T_g, and (PSobMA, PBMA)-based colloids (see Supporting Information Figure S8), exhibit a distribution on the bare Si akin to pure PMMA and PBMA colloids with a PDMAEMA-shell.[34]

"GISAXS (grazing incidence small-angle X-ray scattering) is statistically significant in studying materials. Choosing an incident angle above the critical angle of the materials of the sample enables comprehensive observation of both the surface and bulk states of the sample. The GISAXS pattern is influenced by the shape of nanostructures within a medium. As a result, GISAXS proves to be a valuable tool for monitoring changes in the form of nanostructures inside a material.

When conducted at a synchrotron, GISAXS is particularly advantageous for observing in situ processes without interrupting the ongoing process. The scattering events for various structures in the layer are detected at distinct positions on the detector. This approach allows for the differentiation of fibrils, voids, and large agglomerations within the CNF layer. GISAXS also facilitates a subtle background comparison, which helps

https://doi.org/10.1021/acsanm.4c01302
ACS Appl. Nano Mater. 2024, 7, 10840−10851

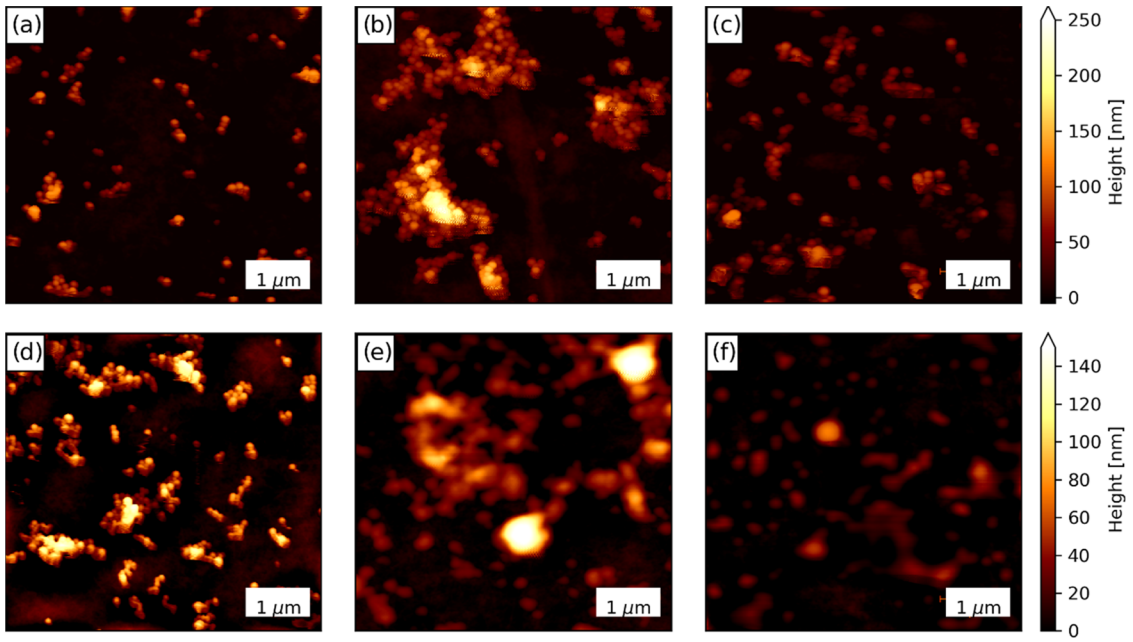

Figure 3. Atomic force microscopy images visualizing the distribution of the colloids on the porous CNF template before annealing in case of (a) $PSobMA_{CTAC}$, (b) $P(SobMA\text{-}co\text{-}BMA)_{1000}$, and (c) $P(SobMA\text{-}co\text{-}BMA)_{CTAC}$, and after annealing at 140 °C in case of (d) $PSobMA_{CTAC}$, (e) $P(SobMA\text{-}co\text{-}BMA)_{1000}$, and (f) $P(SobMA\text{-}co\text{-}BMA)_{CTAC}$.

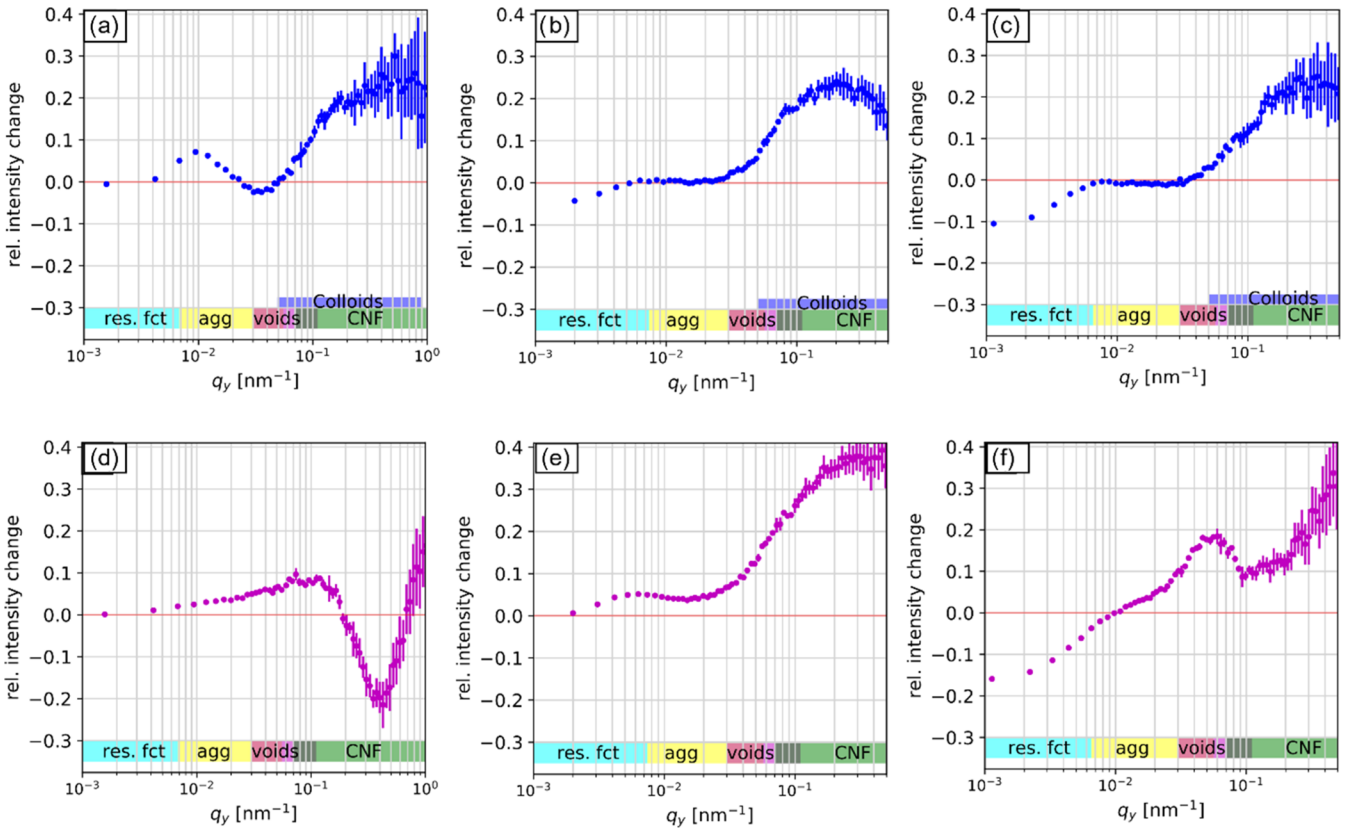

Figure 4. GISAXS data of spray-deposited colloids $P(SobMA\text{-}co\text{-}BMA)_{1000}$ (a, d), $PSobMA_{CTAC}$ (b, e), and $P(SobMA\text{-}co\text{-}BMA)_{CTAC}$ (c, f) on the CNF surface, represented in the relative change format. This representation allows for a comparison of structural changes relative to the pristine CNF layer (see Supporting Information, 1d).

identify the presence of changes in nanostructures within the material."

In 4a, 4b, and 4c, the colloid−CNF hybrid samples are presented under ambient conditions, while 4d, 4e, and 4f showcase the same thin films during the annealing process at 140 °C. Different regimes are marked by CNF agglomerations (Yellow, "agg"), CNF voids (Magenta, "voids"), and CNF bundles (Green, "CNF"). These markers signify the domination

https://doi.org/10.1021/acsanm.4c01302
ACS Appl. Nano Mater. 2024, 7, 10840−10851

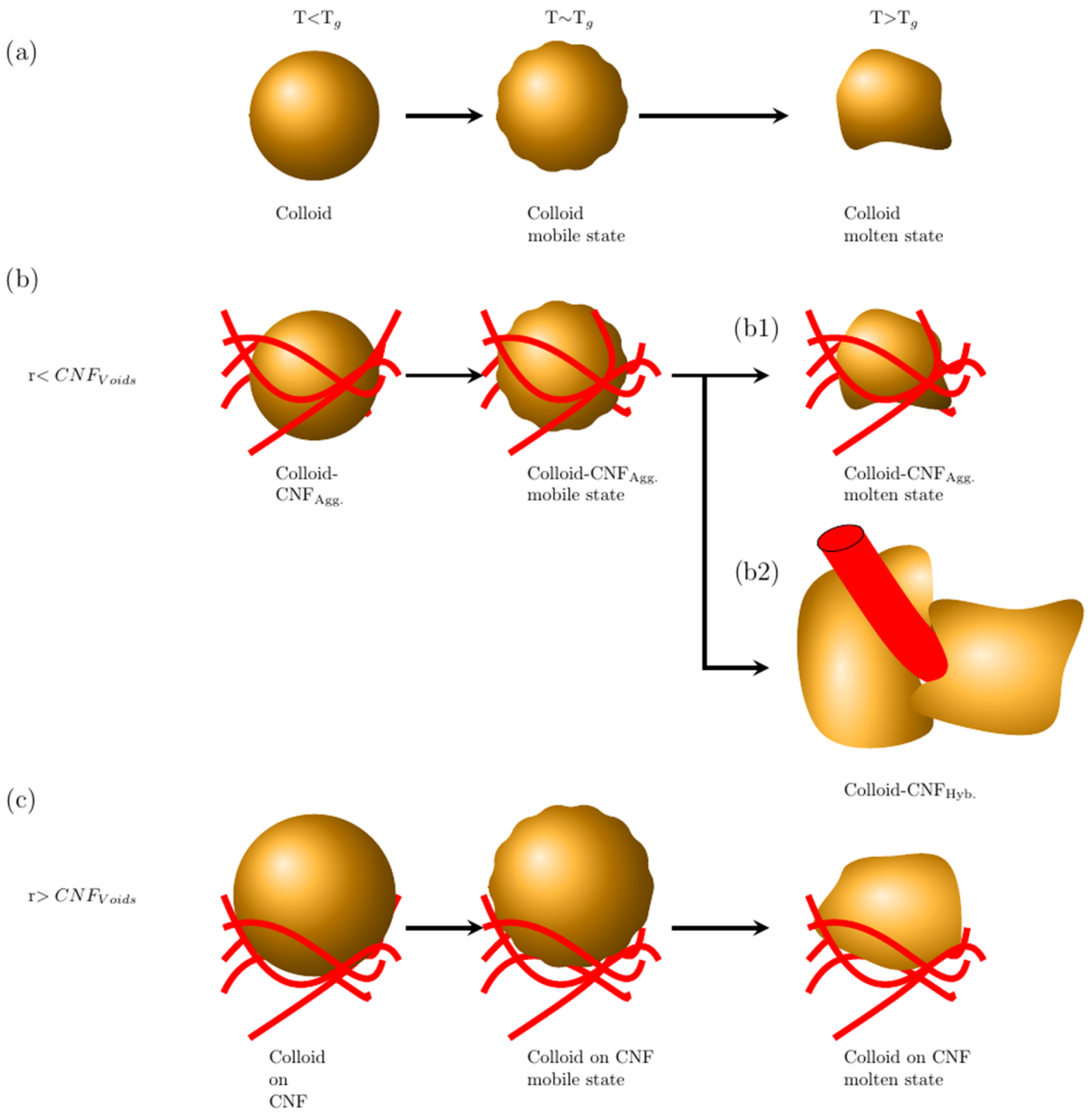

Figure 5. Visualization of the annealing process of a single P(SobMA-*co*-BMA)$_{1000}$ colloid (orange spheres) which is surrounded by CNF due to imbibition. (a) Shape evolution of the colloids, (b) shape evolution of the colloids in the presence of CNF after imbibition, (c) shape the evolution of the colloids without imbibition on top of the CNF layer. (b1) The colloids are surrounded by CNF and (b2) the CNF is surrounded by more than 2 colloids, both together representing the Colloid−CNF$_{Hyb}$ hybrid nanocomposite. (For visibility, (b2) scaled by a factor of 7.) At temperatures below T_g, colloids maintain their shape. If the temperature is equal to T_g, shape changes begin as the colloids enter a mobile phase. The colloids transit into a mobile phase. If the temperature is higher than T_g, the colloid melts imbibes into the CNF network and adheres to the CNF. The melting of the colloids is corroborated by our previous work.[40]

of different structures within the GISAXS data corresponding to the pristine CNF layer. Table S3 summarizes the designation of the colloids and CNF structures together with their corresponding agglomerates.

The blue rectangle identifies the scattering regime of the colloids, derived from the GISAXS data of the colloidal layer deposited on pristine Si. The resolution function (res. fct, cyan) correlates with the beam size and beam divergence, superposing with the scattering of large structures in the scattered intensity for $q_y \leq 6 \times 10^{-3}$ nm^{-1}. The data are logarithmically binned for better visibility, while unbinned data are presented in Figure S9.

Figure 4 depicts the normalized 1D GISAXS cuts in the relative change representation for (PSobMA-*co*-BMA)$_{1000}$, PSobMA$_{CTAC}$, and P(SobMA-*co*-BMA)$_{CTAC,}$ before and after annealing. After spray deposition, the presence of colloids is evidenced in the relative intensity change representation by an increase in the GISAXS signal for $0.05 \leq q_y \leq 0.9$ nm^{-1} for all colloids, P(SobMA-*co*-BMA)$_{1000}$ (Figure 4a), PSobMA$_{CTAC}$ (Figure 4b) and P(SobMA-*co*-BMA)$_{CTAC}$ (Figure 4c).

For P(SobMA-*co*-BMA)$_{1000}$ (Figure 4a), the GISAXS pattern intensity in the q_y range of 0.02 nm$^{-1} \leq q_y \leq 0.06$ nm^{-1} (magenta area) is relatively reduced after colloidal deposition, while in the range of 0.008 nm$^{-1} \leq q_y \leq 0.02$ nm^{-1} (yellow area), the intensity increases. Evident colloid deposition on the CNF surface is marked by a signal increase at high q_y-values, specifically 0.05 nm$^{-1} \leq q_y \leq 1$ nm^{-1} (blue area). The intensity dips observed for 0.02 nm$^{-1} \leq q_y \leq 0.06$ nm^{-1} and 0.006 nm$^{-1} \leq q_y \leq 0.02$ nm^{-1} in the relative intensity representation correspond to CNF void filling and the creation of P(SobMA-*co*-BMA)$_{1000}$-CNF agglomerations, respectively.

In Figure 4b (PSobMA$_{CTAC}$) and Figure 4c (P(SobMA-*co*-BMA)$_{CTAC}$), the relative intensity changes are nearly zero for

https://doi.org/10.1021/acsanm.4c01302
ACS Appl. Nano Mater. 2024, 7, 10840−10851

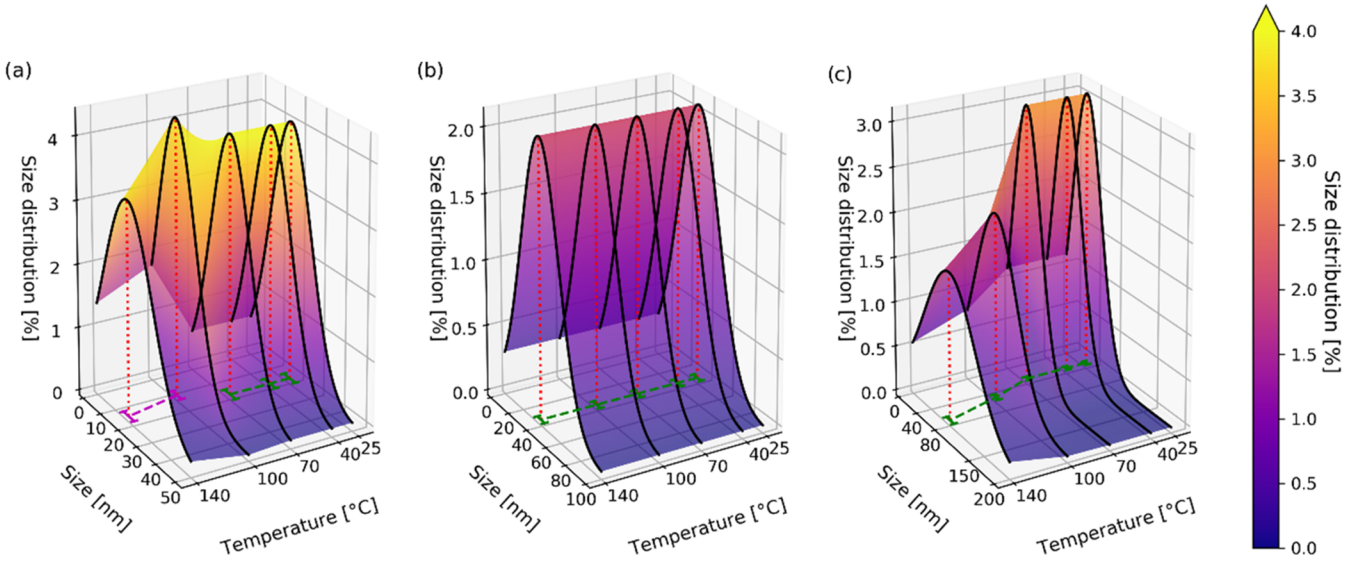

Figure 6. Radii distribution of deposited colloids on the porous CNF network during the annealing process up to 140 °C is observed via GISAXS for (a) P(SobMA-*co*-BMA)$_{1000}$, (b) PSobMA$_{CTAC}$, and (c) P(SobMA-*co*-BMA)$_{CTAC}$. The radii distribution illustrates the evolution of colloid radii during the annealing process. After reaching the glass transition temperature (T_g), the colloids transition into their mobile state and begin to coalesce. P(SobMA-*co*-BMA)$_{1000}$ colloids also initiate coalescence but additionally form a new hybrid nanocomposite ("colloids-CNF$_{Hyb}$") together with the CNF and the CNF$_{Bundles}$ after reaching T_g. In the plots, black graphs represent data points, and the colored surface is the interpolation between the data points. The average radius of the single distribution is marked on the size−temperature plane. Green marks correspond to the radius of the colloidal structure, while magenta marks denote the average radius of the ("colloids-CNF$_{Hyb.}$"). The average radii and the polydispersity index (PDI) are listed in Table 3.

Table 3. Summary of the Properties of the Spray-Deposited Colloids as Evaluated via AFM and GISAXS

	P(SobMA-*co*-BMA)$_{1000}$	PSobMA$_{CTAC}$	P(SobMA-*co*-BMA)$_{CTAC}$
radius$_{AFM}$ [nm]			
after spraying ∼25 °C	26 ± 19	48 ± 20	40 ± 22
after annealing	116 ± 105	50 ± 14	98 ± 79
radius$_{GISAXS}$ [nm]			
after spraying ∼25 °C	20 ± 3	20 ± 3	41 ± 4
during annealing at			
∼40 °C	20 ± 3	39 ± 4	41 ± 4
∼70 °C	20 ± 3	20 ± 3	39 ± 5
∼100 °C	13.5 ± 2.0[a]	40 ± 5	59 ± 5
∼140 °C	17.5 ± 2.5[a]	40 ± 6	82 ± 8
PDI$_{GISAXS}$			
after spraying ∼25 °C	0.32 ± 0.03	0.45 ± 0.04	0.35 ± 0.03
during annealing at			
∼40 °C	0.32 ± 0.03	0.45 ± 0.04	0.35 ± 0.03
∼70 °C	0.32 ± 0.03	0.44 ± 0.04	0.35 ± 0.03
∼100 °C	0.5 ± 0.1[a]	0.43 ± 0.03	0.5 ± 0.1
∼140 °C	0.7 ± 0.1[a]	0.43 ± 0.03	0.6 ± 0.1
imbibition into the CNF layer			
after spraying	yes	no	no
after annealing	yes	no	no
coalescence after annealing	in and on the CNF layer	no	on the CNF surface

[a]Colloid−CNF−hybrid particle.

0.006 nm^{-1} ≤ q_y ≤ 0.06 nm^{-1}. However, for 0.03 nmΛ-1 ≤ q_y ≤ 0.9 nm^{-1}, the relative intensity change is positive, indicating deposition of PSobMA$_{CTAC}$ and P(SobMA-*co*-BMA)$_{CTAC}$ colloids on the CNF surface (strong scattering colloids-air). The negligible relative intensity changes between 0.006 nm^{-1} ≤ q_y ≤ 0.6 nm^{-1} correspond to the absence of colloidal imbibition in the CNF network. PSobMA$_{CTAC}$ and P(SobMA-*co*-BMA)$_{CTAC}$ colloids do not form colloid−CNF agglomerations. The reduction of colloidal agglomerations on porous CNF thin films is akin to the behavior of silver nanoparticles on CNF, where a reduced number of colloidal agglomerates is observed.

During annealing at 140 °C, the polymer chains within P(SobMA-*co*-BMA)$_{1000}$ colloids become more mobile, influenced by the T_g of P(SobMA-*co*-BMA)$_{1000}$, which is 74 °C. As a result, the shape of the P(SobMA-*co*-BMA)$_{1000}$ colloids changes. The relative intensity changes of the annealed P(SobMA-*co*-BMA)$_{1000}$-CNF are negative for 0.2 nm^{-1} ≤ q_y ≤ 0.9 nm^{-1} and positive for 0.006 nm^{-1} ≤ q_y ≤ 0.2 nm^{-1}.

https://doi.org/10.1021/acsanm.4c01302
ACS Appl. Nano Mater. 2024, 7, 10840−10851

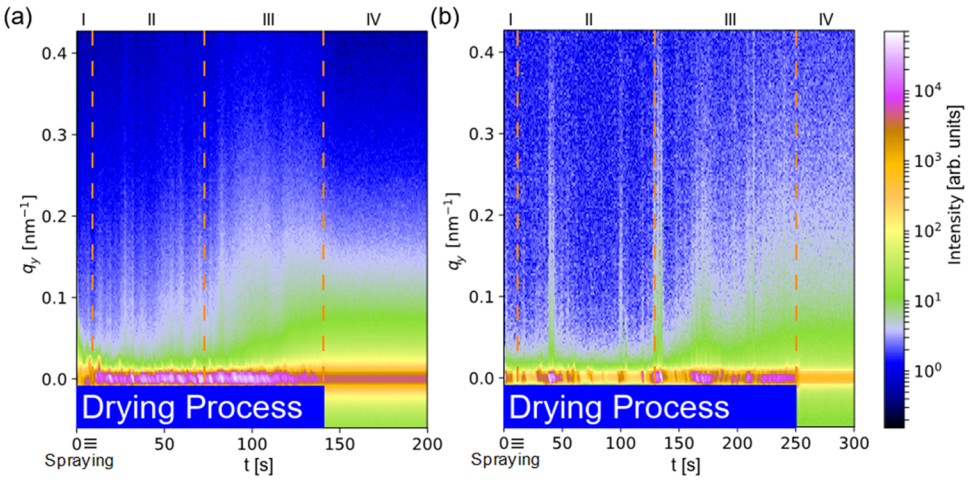

Figure 7. Formation of the P(SobMA-*co*-BMA)$_{1000}$ colloidal layer on top of (a) the CNF layer and (b) the nonporous Si wafer is monitored as a function of drying time observed with GISAXS. In the mapping presentation, the horizontal line cuts from the 2D GISAXS data are displayed as a function of q_y and time. The reference time ($t \equiv 0$ s) corresponds to the spray deposition and the start of the drying process of the first spray pulse. The drying process of the spray-deposited colloidal layer is finished for CNF after 140 ± 5 s and for deposition on silicon after 250 ± 10 s.

The negative intensity changes in the range 0.2 nm^{-1} ≤ q_y ≤ 0.9 nm^{-1} suggest a reduced number of particles in the size range of both CNF$_{Bundles}$ and P(SobMA-*co*-BMA)$_{1000}$ colloids. On the other hand, the positive intensity change corresponds to a size range slightly larger than the size of CNF$_{Bundles}$ and slightly smaller than the size of the P(SobMA-*co*-BMA)$_{1000}$ colloids. This indicates interactions between P(SobMA-*co*-BMA)$_{1000}$ colloids and CNF$_{Bundles}$ after reaching the T_g of the colloids.

Hence, the GISAXS data reveals the formation of a nanocomposite of P(SobMA-*co*-BMA)$_{1000}$ and CNF$_{Bundles}$ due to the coalescence of CNF bundles and mobile polymer colloids. The colloids, surrounded by CNF through imbibition, foster the hybrid formation. These structures are named colloids-CNF$_{Hyb.}$, as visualized in Figure 5.

During the annealing process, the PSobMA$_{CTAC}$ colloids maintain their shape. The GISAXS data in Figure 4e indicates neither imbibition of colloids into the CNF (no negative relative intensity values between 0.02 nm^{-1} ≤ q_y ≤ 0.06 nm^{-1}) nor coalescence of the colloids during annealing (which would be visible in the range 0.008 nm^{-1} ≤ q_y ≤ 0.02 nm^{-1}).

In the case of P(SobMA-*co*-BMA)$_{CTAC}$, a positive relative intensity change is observed for q_y ≥ 0.01 nm^{-1} (Figure 4f). Agglomerations of only colloids are formed solely on the CNF surface, with no penetration into the CNF network. Thus, for both PSobMA$_{CTAC}$ (Figure 4e) and P(SobMA-*co*-BMA)$_{CTAC}$ (Figure 4f) colloids, no formation of agglomerations with CNF is observed.

The size evolution during the annealing of the colloids is depicted in Figure 6. After reaching the T_g for P(SobMA-*co*-BMA)$_{1000}$ colloids (Figure 6a), these colloids coalesce and form a hybrid material with the fibrils and the CNF bundles in and on the CNF layer. Their size is indicated by the magenta line in Figure 6a. The colloid−colloid coalescence on the pristine Si wafer is shown in Figure S10.

In the case of PSobMA$_{CTAC}$ (Figure 6b), the colloids do not coalesce at all nor change their shape or size during the annealing process. For P(SobMA-*co*-BMA)$_{CTAC}$ (Figure 6c), the colloids coalesce only on the surface of the CNF film or the silicon surface. Hence, the PSobMA$_{CTAC}$ and P(SobMA-*co*-BMA)$_{CTAC}$ colloids do not form hybrid nanocomposite colloids-CNF$_{Hyb.}$

The coalescence of the colloids (PSobMA$_{CTAC}$ and P(SobMA-*co*-BMA)$_{CTAC}$) is visible in the AFM images (Figure 3) and the size evolution via GISAXS; see Figure 5b,c. Table 3 summarizes the findings concerning coalescence and imbibition. The coalesce of P(SobMA-*co*-BMA)$_{1000}$ with the CNF into a nanocomposite inside the network is the reason why the surface energy for the annealed P(SobMA-*co*-BMA)$_{1000}$ CNF hybrid material is slightly smaller than for the pristine CNF layer. The P(SobMA-*co*-BMA)$_{1000}$ colloids more effectively penetrate the CNF layer due to annealing, making the CNF more visible at the colloid−CNF surface toward the air.

The formation of the colloidal layer during the drying process is tracked in situ via GISAXS, as illustrated in Figure 7. After the deposition of colloidal inks, water evaporation commences. The drying dynamics of the CNF surface after each pulse are influenced by humidity (RH = 35 ± 2%), surface temperature (25 ± 2 °C), liquid volume (20 ± 2 μL), and the topology of the underlying substrate.

The CNF layer exhibits a nonstructured network, allowing water and smaller colloids to penetrate during spray deposition. The drying of the CNF layer added during one spray pulse is completed after 140 ± 10 s, while on the Si wafer (Figure 7b), the drying process concludes after 250 ± 10 s. Water is imbibed into the CNF layer, and the water on the CNF surface evaporates faster than on the silicon surface.

Immediately after deposition, droplets of the colloidal ink on the CNF and Si wafer coalesce into a liquid film on top of the surface, marking the initial phase of the drying process (I). After the droplets' coalescence (9 ± 2 s on the CNF layer and 11 ± 2 s on the Si wafer), the sample surface is covered with the deposited liquid dispersion. In this phase, water evaporates, and colloids move freely in the liquid. This second phase (II) of the drying process takes 117 ± 10 s for the bare Si wafer and 64 ± 5 s for the CNF film.

The third phase (III) of the drying process starts when the colloids begin to interact with each other, and the colloidal layer develops. In this phase, sufficient water is evaporated, and only a thin water film remains. Eventually, the water evaporates, and the colloidal layer forms on top of the surface. The evaporation of water ensures that the colloids form agglomerations during this process.

https://doi.org/10.1021/acsanm.4c01302
ACS Appl. Nano Mater. 2024, 7, 10840−10851

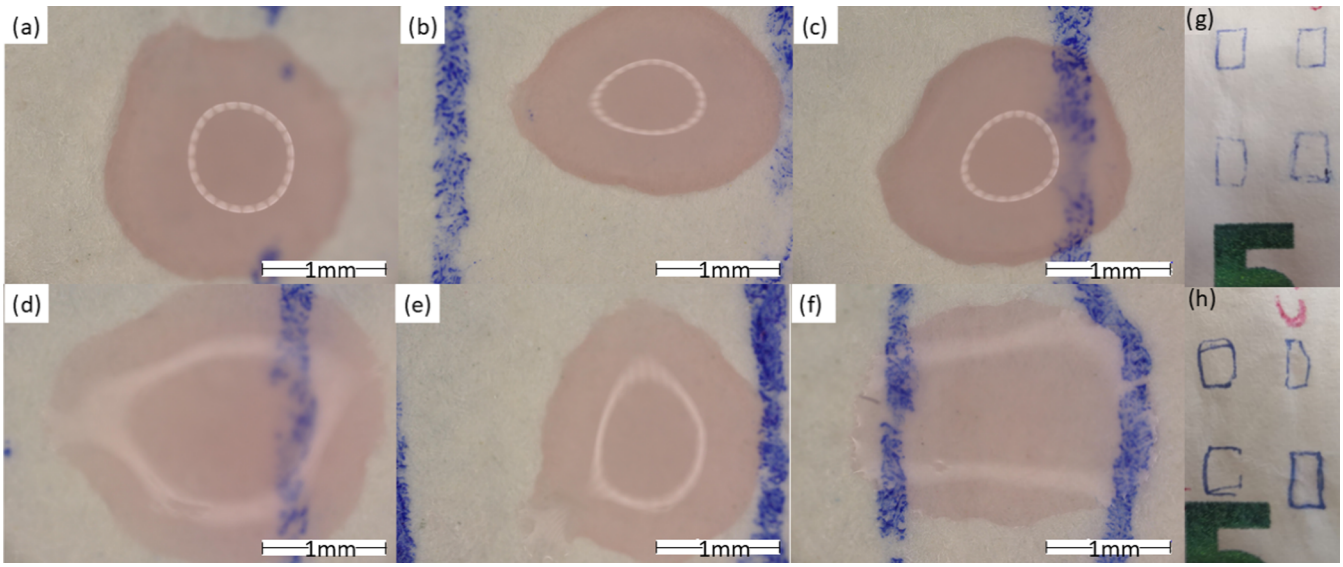

Figure 8. Optical microscopy images of 0.5 μL water droplets on a 5 € note: The water is colored red for improved visibility. (a) Pristine 5 € note, modified with (b) P(SobMA-*co*-BMA)$_{1000}$, (c) P(SobMA-*co*-BMA)$_{1000}$ after annealing, (d) pure CNF layer, (e) CNF together with P(SobMA-*co*-BMA)$_{1000}$, and (f) CNF together with P(SobMA-*co*-BMA)$_{1000}$ after annealing. The 5 € notes ((g) unannealed and (h) annealed) were coated from (up, left) to (down, right) with [Colloids, CNF + colloids, pristine, CNF]. The scale bar corresponds to 1 mm. The blue lines in (a–f) are markers for the author to put the water droplet at the right positions of the 5 € note (g, h). The white circle in the droplet is the reflection of the microscope lamp.

Phases I, II, III, and IV are comparable with phases 2, 3, 4, and 5 observed in previous work by Zhang et al.[45] Due to the topology of the CNF layer, the colloids, which are smaller than the CNF void structure, and the water itself have penetrated the CNF layer (see Figure 4a). The colloidal layer comprises individual single colloids and their agglomerations. In the context of sustainability, it is crucial for anticounterfeiting features to be derived from renewable resources. Therefore, in this work spray-deposited sustainable wood-based colloidal inks are used to alter the hydrophilic characteristics of porous CNF thin films. This is useful to prove the exactness of the biobased surface. This work presents three possibilities to prove the trueness of a modified paper. The trueness can be proved by the spreading of a simple droplet, the scanning of the nanostructure, and the X-ray scattering with the nanostructure.

The surface's water-wetting behavior and imbibition are intricately linked by the surface energy, which is altered by the presence of colloids within the CNF network. The choice of colloidal material (PSobMA$_{CTAC}$, P(SobMA-*co*-BMA)$_{1000}$, P-(SobMA-*co*-BMA)) and the corresponding annealing process are pivotal factors influencing this modification in surface energy. Colloid deposition leads to a significant reduction in the surface energy of the CNF layer, reminiscent of the effects observed with PMMA polymers sharing a similar core–shell colloidal structure. Notably, P(SobMA-*co*-BMA)$_{1000}$ emerges as a promising candidate for paper modification.

The surface energy manifests itself when the test surface is exposed to a water droplet, providing a means to detect any missing process steps in the surface modification. Generally, the surface energy of the CNF-colloid hybrid material exhibits a slight increase after the annealing process, with the exception of P(SobMA-*co*-BMA)$_{1000}$, which maintains a similarity to pristine CNF (Figure 2). This observation underscores the intricate interplay between colloidal material, annealing conditions, and surface energy modifications in the development of sustainable, wood-based anticounterfeiting features.

The interaction between a water droplet and different surfaces provides visual insights into surface properties. Water behavior is contingent upon the surface material, prompting the modification of the surface such as, for example, a 5 € note using the same treatment as described for the silicon wafer. The topologies of the colloidal layer, CNF layer, and CNF-colloidal layer are presumed to be to a large extent independent of the substrate material, such as silicon or a 5 € note. Optical microscopy images (Figure 8) reveal different droplet types, presenting two identification features for anticounterfeiting, namely, the droplet shape and the optical thickness. For higher surface energies, the water droplet of 0.5 μL is brighter. This shape corresponds to a flatter droplet and the droplet has spread further on the surface and the covered surface is higher (see Table 4). The water adhesion results on the 5 € agree with the surface energy (Figure 2) and the contact angles results (Figure S7)

The pure CNF (Figure 8d) and the annealed colloids on CNF (Figure 8f) have a higher surface charge than the 5 € surface (Figure 8a), the colloidal surface (Figure 8b), the colloidal surface after the annealing (Figure 8d), and the colloidal surface on CNF without annealing (Figure 8e).

Table 4. Calculated Contact Angles and Surface Energies form the Optical Microscope Images in Figure 8

	avg. radius of the droplet [mm]	contact angle [deg]	surface energy [mN/m]
pristine 5 € note	0.85 ± 0.05	70 ± 5	32 ± 5
P(SobMA-*co*-BMA)$_{1000}$	0.9 ± 0.05	65 ± 5	37 ± 5
P(SobMA-*co*-BMA)$_{1000}$ after annealing	0.9 ± 0.05	65 ± 5	37 ± 5
CNF layer	1.2 ± 0.1	11 ± 3	71 ± 2
CNF together with P(SobMA-*co*-BMA)$_{1000}$	0.95 ± 0.06	50 ± 3	49 ± 3
CNF together with P(SobMA-*co*-BMA)$_{1000}$ after annealing	1 ± 0.08	22 ± 4	68 ± 2

https://doi.org/10.1021/acsanm.4c01302
ACS Appl. Nano Mater. 2024, 7, 10840–10851

By distinguishing the water droplets, it is possible to recognize whether colloids and/or CNF have been applied to the surface of the object and whether the system has been tempered.

CONCLUSIONS

The deposition of the utilized colloids ($PSobMA_{CTAC}$, $P(SobMA\text{-}co\text{-}BMA)_{1000}$, $P(SobMA\text{-}co\text{-}BMA)_{CTAC}$) induces modifications in the surface energy of the TEMPO−CNF layer. Additionally, annealing the CNF-colloidal system brings about further alterations in surface energy. The shifts in surface energy are closely linked to morphological changes occurring during the deposition and annealing processes, which are discernible in the corresponding AFM and compared GISAXS data. AFM distinguishes if the colloids are present on the CNF surface and if the colloids are unannealed or annealed. Thereby the AFM reveals a random distribution of colloids on the CNF surface. At the same time, GISAXS differentiates between imbibition and the absence of colloids inside the CNF layer.

The nonzero difference in the compared GISAXS data is attributed to the morphological change.

The nonzero difference following deposition of colloids can be ascribed to the presence of colloids on the CNF surface, the filling of CNF voids with colloids, and the creation of agglomerations comprising colloids and CNF. Notably, the behavior of P(SobMA-*co*-BMA)1000 colloids illustrates that colloids with a smaller radius than the CNF voids can infiltrate the CNF layer during deposition. Subsequently, during annealing, these colloids undergo coalescence with other colloids and the CNF.

On the other hand, observations from $P(SobMA\text{-}co\text{-}BMA)_{CTAC}$ highlight that colloids with a larger radius than the CNF voids do not imbibe the CNF layer; instead, they coalesce on the surface. Consequently, the morphological changes observed can be attributed to the coalescence of colloids on and within the CNF layer.

This project establishes that the water adhesion of porous thin films of CNF is modifiable through the spray deposition of colloidal inks on the CNF layer surface and subsequent annealing. Furthermore, it demonstrates that the imbibition of colloids into a porous film and resultant morphological changes are observable through GISAXS. The combination of surface energy, and AFM serves as a nontrivial comprehensive validity series. A water droplet test indicates the correctness of surface energy, and AFM reveals the presence of the colloids or the impact of the annealing process.

ASSOCIATED CONTENT

Supporting Information

The Supporting Information is available free of charge at https://pubs.acs.org/doi/10.1021/acsanm.4c01302.

> Surface energy changes influenced by deposition of colloids and the thermal treatment (S1), AFM image showing the structure distribution of colloids (S2), GISAXS study of structure formation during thermal treatment (S3), and time-resolved GISAXS study of structure formation during evaporation (S4) (PDF)

AUTHOR INFORMATION

Corresponding Author

Stephan V. Roth − *Deutsches Elektronen-Synchrotron DESY, 22607 Hamburg, Germany; Department of Fibre and Polymer Technology, KTH Royal Institute of Technology, SE-10044 Stockholm, Sweden;* orcid.org/0000-0002-6940-6012; Email: stephan.roth@desy.de, svroth@kth.se

Authors

Constantin Harder − *Deutsches Elektronen-Synchrotron DESY, 22607 Hamburg, Germany; TUM School of Natural Sciences, Department of Physics, Chair for Functional Materials, Technical University of Munich, 85748 Garching, Germany;* orcid.org/0000-0001-5857-0522

Marie Betker − *Deutsches Elektronen-Synchrotron DESY, 22607 Hamburg, Germany; Department of Fibre and Polymer Technology, KTH Royal Institute of Technology, SE-10044 Stockholm, Sweden;* orcid.org/0000-0001-6465-2188

Alexandros E. Alexakis − *Department of Fibre and Polymer Technology, KTH Royal Institute of Technology, SE-10044 Stockholm, Sweden; Wallenberg Wood Science Center (WWSC), KTH Royal Institute of Technology, SE-10044 Stockholm, Sweden;* orcid.org/0000-0001-8317-3529

Yusuf Bulut − *Deutsches Elektronen-Synchrotron DESY, 22607 Hamburg, Germany; TUM School of Natural Sciences, Department of Physics, Chair for Functional Materials, Technical University of Munich, 85748 Garching, Germany;* orcid.org/0000-0003-0090-3990

Benedikt Sochor − *Deutsches Elektronen-Synchrotron DESY, 22607 Hamburg, Germany*

L. Daniel Söderberg − *Department of Fibre and Polymer Technology, KTH Royal Institute of Technology, SE-10044 Stockholm, Sweden; Wallenberg Wood Science Center (WWSC), KTH Royal Institute of Technology, SE-10044 Stockholm, Sweden;* orcid.org/0000-0003-3737-0091

Eva Malmström − *Department of Fibre and Polymer Technology, KTH Royal Institute of Technology, SE-10044 Stockholm, Sweden; Wallenberg Wood Science Center (WWSC), KTH Royal Institute of Technology, SE-10044 Stockholm, Sweden;* orcid.org/0000-0002-8348-2273

Peter Müller-Buschbaum − *TUM School of Natural Sciences, Department of Physics, Chair for Functional Materials, Technical University of Munich, 85748 Garching, Germany; Heinz Maier-Leibnitz-Zentrum (MLZ), Technical University of Munich, 85748 Garching, Germany;* orcid.org/0000-0002-9566-6088

Complete contact information is available at: https://pubs.acs.org/10.1021/acsanm.4c01302

Notes

The authors declare no competing financial interest.

ACKNOWLEDGMENTS

C.H. acknowledges the DESY innovation fund for funding the project “Interaction of complex fluids with porous media”. M.B. and S.V.R. thank DSF under the grant, DSF-33, “Investigation of processes for fabricating functional multicomponent stacks based on nano paper and spray-coating” for funding. A.E.A. and E.M. acknowledge funding from the Knut and Alice Wallenberg Foundation (KAW) through the Wallenberg Wood Science Center (WWSC 2.0: KAW 2018.0452). P.M.-B. was supported by Deutsche Forschungsgemeinschaft (DFG) with funding via Germany’s Excellence Strategy-EXC 2089/1-390776260 (e-conversion) and the International Research Training Group 2022 Alberta/Technical University of Munich International Graduate School for Environmentally Responsible Functional Hybrid Materials (ATUMS). The authors acknowledge DESY (Hamburg, Germany), a member of the Helmholtz Association

HGF, for the provision of experimental facilities. Parts of this research are carried out at PETRA III, and the authors thank Matthias Schwartzkopf, Andrei Chumakov, and in particular Jan Rubeck, for assistance in using P03. Beamtime is allocated for proposals I-20010005 and I-20191361 EC.

REFERENCES

(1) Nguyen, N. N.; Lee, H. C.; Baek, K.; Yoo, M. S.; Lee, H.; Lim, H.; Choi, S.; Kim, C. J.; Nam, S. W.; Cho, K. Atomically Smooth Graphene-Based Hybrid Template for the Epitaxial Growth of Organic Semiconductor Crystals. *Adv. Funct. Mater.* **2021**, *31* (11), No. 2008813.

(2) Zhang, Y.; Zhang, T.; Huang, Z.; Yang, J. A New Class of Electronic Devices Based on Flexible Porous Substrates. *Adv. Sci.* **2022**, *9* (7), No. 2105084.

(3) Hridya, T.; Varghese, E.; Harikumar, P. S. Removal of Heavy Metals from Aqueous Solution Using Porous (Styrene-Divinylbenzene)/CuNi Bimetallic Nanocomposite Microspheres. *Environ. Nanotechnol., Monit. Manage.* **2021**, *16* (July), No. 100606.

(4) Kalaburgi, B.; Daruka Prasad, B.; Lavanya, D. R.; Sharma, S. C.; Srikanth, C.; Darshan, G. P.; Nasreen Taj, M.; Premkumar; Nagabhushana, H. Facile and Eco-Friendly PVA Nanocomposites as a Photo-Luminescent: Anti-Counterfeiting, LED and Wettability Applications. *Ceram. Int.* **2023**, *49* (3), 4586−4598.

(5) Quan, Z.; Zhang, Q.; Li, H.; Sun, S.; Xu, Y. Fluorescent Cellulose-Based Materials for Information Encryption and Anti-Counterfeiting. *Coord. Chem. Rev.* **2023**, *493* (June), No. 215287.

(6) Maestro, A.; Guzmán, E.; Ortega, F.; Rubio, R. G. Contact Angle of Micro- and Nanoparticles at Fluid Interfaces. *Curr. Opin. Colloid Interface Sci.* **2014**, *19* (4), 355−367.

(7) Chen, A. X.; Lau, H. Y.; Teo, J. Y.; Wang, Y.; Choong, D. Z. Y.; Wang, Y.; Luo, H. K.; Yang, Y. Y.; Li, N. Water-Mediated In Situ Fabrication of CuI Nanoparticles on Flexible Cotton Fabrics as a Sustainable and Skin-Compatible Coating with Broad-Spectrum Antimicrobial Efficacy. *ACS Appl. Nano Mater.* **2023**, *6*, 13238−13249.

(8) Li, L.; Chen, P.; Medina, L.; Yang, L.; Nishiyama, Y.; Berglund, L. A. Residual Strain and Nanostructural Effects during Drying of Nanocellulose/Clay Nanosheet Hybrids: Synchrotron X-Ray Scattering Results. *ACS Nano* **2023**, *17* (16), 15810−15820.

(9) Von Bohlen Und Halbach, O. Analysis of Morphological Changes as a Key Method in Studying Psychiatric Animal Models. *Cell Tissue Res.* **2013**, *354*, 41−50.

(10) Ghafouri, V.; Ebrahimzad, A.; Shariati, M. The Effect of Annealing Time and Temperature on Morphology and Optical Properties of ZnO Nanostructures Grown by a Self-Assembly Method. *Sci. Iran.* **2013**, *20* (3), 1039−1048.

(11) Fujisawa, S.; Daicho, K.; Yurtsever, A.; Fukuma, T.; Saito, T. Morphological Changes of Polymer-Grafted Nanocellulose during a Drying Process. *Biomacromolecules* **2023**, *24*, 3908−3916.

(12) Betker, M.; Harder, C.; Erbes, E.; Heger, J. E.; Alexakis, A. E.; Sochor, B.; Chen, Q.; Schwartzkopf, M.; Körstgens, V.; Müller-Buschbaum, P.; Schneider, K.; Techert, S. A.; Söderberg, L. D.; Roth, S. V. Sprayed Hybrid Cellulose Nanofibril − Silver Nanowire Transparent 2 Electrodes for Organic Electronic Applications. *ACS Appl. Nano Mater.* **2023**, *6* (14), 13677−13688.

(13) Chen, Q.; Betker, M.; Harder, C.; Brett, C. J.; Schwartzkopf, M.; Ulrich, N. M.; Toimil-Molares, M. E.; Trautmann, C.; Söderberg, L. D.; Weindl, C. L.; Körstgens, V.; Müller-Buschbaum, P.; Ma, M.; Roth, S. V. Biopolymer-Templated Deposition of Ordered and Polymorph Titanium Dioxide Thin Films for Improved Surface-Enhanced Raman Scattering Sensitivity. *Adv. Funct. Mater.* **2022**, *32* (6), No. 2108556.

(14) Moon, C.; Pujar, P.; Gandla, S.; So, B.; Lee, S.; Kim, D.; Kwon, K.; Kim, S. Anticounterfeiting Tags Based on Randomly Oriented MoSx Clusters Enabled by Capillary and Marangoni Flow. *Commun. Mater.* **2023**, *4* (98), 1−9, DOI: 10.1038/s43246-023-00424-w.

(15) Su, X.; Li, K.; Xie, H.; Chen, Z.; Li, X.; Wu, W. Controllable Hydrophilic/Superhydrophobic Patterned Coatings for Optical Information Encryption/Decryption Based on Water-Triggered Opaque to Translucent Transition. *J. Colloid Interface Sci.* **2024**, *654* (PA), 764−773.

(16) Brett, C. J.; Mittal, N.; Ohm, W.; Gensch, M.; Kreuzer, L. P.; Körstgens, V.; Månsson, M.; Frielinghaus, H.; Müller-Buschbaum, P.; Söderberg, L. D.; Roth, S. V. Water-Induced Structural Rearrangements on the Nanoscale in Ultrathin Nanocellulose Films. *Macromolecules* **2019**, *52* (12), 4721.

(17) Lefebvre, A. H.; McDonell, V. G.*Atomization and Sprays*; CRC Press, 2017 DOI: 10.1201/9781315120911.

(18) Abu Jarad, N.; Imran, H.; Imani, S. M.; Didar, T. F.; Soleymani, L. Fabrication of Superamphiphobic Surfaces via Spray Coating; a Review. *Adv. Mater. Technol.* **2022**, *7* (10), No. 2101702.

(19) Chen, Q.; Brett, C. J.; Chumakov, A.; Gensch, M.; Schwartzkopf, M.; Körstgens, V.; Söderberg, L. D.; Plech, A.; Zhang, P.; Müller-Buschbaum, P.; Roth, S. V. Layer-by-Layer Spray-Coating of Cellulose Nanofibrils and Silver Nanoparticles for Hydrophilic Interfaces. *ACS Appl. Nano Mater.* **2021**, *4*, 503−513.

(20) Mahendra, I. P.; Wirjosentono, B.; Tamrin; Ismail, H.; Mendez, J. A. Thermal and Morphology Properties of Cellulose Nanofiber from TEMPO-Oxidized Lower Part of Empty Fruit Bunches (LEFB). *Open Chem.* **2019**, *17* (1), 526−536.

(21) Kelly, P. V.; Cheng, P.; Gardner, D. J.; Gramlich, W. M. Aqueous Polymer Modification of Cellulose Nanofibrils by Grafting-Through a Reactive Methacrylate Group. *Macromol. Rapid Commun.* **2021**, *42* (3), No. 2000531.

(22) Rosén, T.; He, H. R.; Wang, R.; Zhan, C.; Chodankar, S.; Fall, A.; Aulin, C.; Larsson, P. T.; Lindström, T.; Hsiao, B. S. Cross-Sections of Nanocellulose from Wood Analyzed by Quantized Polydispersity of Elementary Microfibrils. *ACS Nano* **2020**, *14* (12), 16743−16754.

(23) Roy, S.; Ghosh, B. D.; Goh, K. L.; Muthoka, R. M.; Kim, J. Modulation of Interfacial Interactions toward Strong and Tough Cellulose Nanofiber-Based Transparent Thin Films with Antifogging Feature. *Carbohydr. Polym.* **2022**, *278*, No. 118974.

(24) Geng, L.; Mittal, N.; Zhan, C.; Ansari, F.; Sharma, P. R.; Peng, X.; Hsiao, B. S.; Söderberg, L. D. Understanding the Mechanistic Behavior of Highly Charged Cellulose Nanofibers in Aqueous Systems. *Macromolecules* **2018**, *51* (4), 1498−1506.

(25) Sanchez-Salvador, J. L.; Campano, C.; Negro, C.; Monte, M. C.; Blanco, A. Increasing the Possibilities of TEMPO-Mediated Oxidation in the Production of Cellulose Nanofibers by Reducing the Reaction Time and Reusing the Reaction Medium. *Adv. Sustainable Syst.* **2021**, *5* (4), No. 2000277.

(26) Zheng, G.; Cui, Y.; Karabulut, E.; Wågberg, L.; Zhu, H.; Hu, L. Nanostructured Paper for Flexible Energy and Electronic Devices. *MRS Bull.* **2013**, *38* (4), 320−325.

(27) Gan, P. G.; Sam, S. T.; Abdullah, M. F. bin.; Omar, M. F. Thermal Properties of Nanocellulose-reinforced Composites. *J. Appl. Polym. Sci.* **2020**, *137*, No. 48544, DOI: 10.1002/app.48544.

(28) Raghuwanshi, V. S.; Garnier, G. Cellulose Nano-Films as Bio-Interfaces. *Front. Chem.* **2019**, *7* (July), 535.

(29) Mietner, J. B.; Jiang, X.; Edlund, U.; Saake, B.; Navarro, J. R. G. 3D Printing of a Bio-Based Ink Made of Cross-Linked Cellulose Nanofibrils with Various Metal Cations. *Sci. Rep.* **2021**, *11* (1), No. 6461, DOI: 10.1038/s41598-021-85865-4.

(30) Aljohani, M. M. Preparation of Polylactic Acid Reinforced with Cellulose Nanofibers toward Photochromic Self-Healing Adhesive for Anti-Counterfeiting Applications. *Int. J. Biol. Macromol.* **2024**, *259* (0141−8130), No. 129065, DOI: 10.1016/j.ijbiomac.2023.129065.

(31) Alexakis, A. E.; Engström, J.; Stamm, A.; Riazanova, A. V.; Brett, C. J.; Roth, S. V.; Syrén, P. O.; Fogelström, L.; Reid, M. S.; Malmström, E. Modification of Cellulose through Physisorption of Cationic Bio-Based Nanolatexes - Comparing Emulsion Polymerization and RAFT-Mediated Polymerization-Induced Self-Assembly. *Green Chem.* **2021**, *23* (5), 2113−2122.

(32) D'Agosto, F.; Rieger, J.; Lansalot, M. RAFT-Mediated Polymerization-Induced Self-Assembly. *Angew. Chem., Int. Ed.* **2020**, *59* (22), 8368−8392.

(33) Song, Y.; Phipps, J.; Zhu, C.; Ma, S. Porous Materials for Water Purification. *Angew. Chem., Int. Ed.* **2023**, *62* (11), No. e202216724.

(34) Engström, J.; Brett, C. J.; Körstgens, V.; Müller-Buschbaum, P.; Ohm, W.; Malmström, E.; Roth, S. V. Core−Shell Nanoparticle Interface and Wetting Properties. *Adv. Funct. Mater.* **2020**, *30* (15), No. 1907720.
(35) Wang, W.; Schaffer, C. J.; Song, L.; Körstgens, V.; Pröller, S.; Indari, E. D.; Wang, T.; Abdelsamie, A.; Bernstorff, S.; Müller-Buschbaum, P. In Operando Morphology Investigation of Inverted Bulk Heterojunction Organic Solar Cells by GISAXS. *J. Mater. Chem. A* **2015**, *3*, 8324−8331.
(36) Koshkina, O.; Raju, L. T.; Kaltbeitzel, A.; Riedinger, A.; Lohse, D.; Zhang, X.; Landfester, K. Surface Properties of Colloidal Particles Affect Colloidal Self-Assembly in Evaporating Self-Lubricating Ternary Droplets. *ACS Appl. Mater. Interfaces* **2022**, *14*, 2275−2290.
(37) Brett, C. J.; Forslund, O. K.; Nocerino, E.; Kreuzer, L. P.; Widmann, T.; Porcar, L.; Yamada, N. L.; Matsubara, N.; Månsson, M.; Müller-Buschbaum, P.; Söderberg, L. D.; Roth, S. V. Humidity-Induced Nanoscale Restructuring in PEDOT:PSS and Cellulose Nanofibrils Reinforced Biobased Organic Electronics. *Adv. Electron. Mater.* **2021**, *7* (6), No. 2100137.
(38) Ohm, W.; Rothkirch, A.; Pandit, P.; Körstgens, V.; Müller-Buschbaum, P.; Rojas, R.; Yu, S.; Brett, C. J.; Söderberg, D. L.; Roth, S. V. Morphological Properties of Airbrush Spray-Deposited Enzymatic Cellulose Thin Films. *J. Coatings Technol. Res.* **2018**, *15* (4), 759−769.
(39) Engström, J.; Hatton, F. L.; Wågberg, L.; D'Agosto, F.; Lansalot, M.; Malmström, E.; Carlmark, A. Soft and Rigid Core Latex Nanoparticles Prepared by RAFT-Mediated Surfactant-Free Emulsion Polymerization for Cellulose Modification − a Comparative Study. *Polym. Chem.* **2017**, *8* (6), 1061.
(40) Harder, C.; Alexakis, A. E.; Bulut, Y.; Xiong, S.; Sochor, B.; Pan, G.; Zhong, H.; Goordeyeva, K.; Reus, M. A.; Körstgens, V.; Jeromin, A.; Keller, T. F.; Söderberg, L. D.; Malmström, E.; Müller-Buschbaum, P.; Roth, S. V. Optical Properties of Slot-Die Coated Hybrid Colloid/Cellulose-Nanofibril Thin Films. *Adv. Opt. Mater.* **2023**, *11* (13), No. 2203058.
(41) Nečas, D.; Klapetek, P. Gwyddion: An Open-Source Software for SPM Data Analysis. *Cent. Eur. J. Phys.* **2012**, *10* (1), 181−188.
(42) Isa, L.; Lucas, F.; Wepf, R.; Reimhult, E. Measuring Single-Nanoparticle Wetting Properties by Freeze-Fracture Shadow-Casting Cryo-Scanning Electron Microscopy. *Nat. Commun.* **2011**, *2* (1), No. 438, DOI: 10.1038/ncomms1441.
(43) De Gennes, P. G. Wetting: Statics and Dynamics. *Rev. Mod. Phys.* **1985**, *57* (3), 827−863.
(44) Herzog, G.; Abul Kashem, M. M.; Benecke, G.; Buffet, A.; Gehrke, R.; Perlich, J.; Schwartzkopf, M.; Körstgens, V.; Meier, R.; Niedermeier, M. A.; Rawolle, M.; Ruderer, M. A.; Müller-Buschbaum, P.; Wurth, W.; Roth, S. V. Influence of Nanoparticle Surface Functionalization on the Thermal Stability of Colloidal Polystyrene Films. *Langmuir* **2012**, *28* (21), 8230−8237.
(45) Zhang, P.; Santoro, G.; Yu, S.; Vayalil, S. K.; Bommel, S.; Roth, S. V. Manipulating the Assembly of Spray-Deposited Nanocolloids: In Situ Study and Monolayer Film Preparation. *Langmuir* **2016**, *32* (17), 4251−4258.

https://doi.org/10.1021/acsanm.4c01302
ACS Appl. Nano Mater. 2024, 7, 10840−10851